

Intensification and spatial homogenization of coastal upwelling under climate change

Daiwei Wang¹, Tarik C. Gouhier², Bruce A. Menge³ & Auroop R. Ganguly¹

The timing and strength of wind-driven coastal upwelling along the eastern margins of major ocean basins regulate the productivity of critical fisheries and marine ecosystems by bringing deep and nutrient-rich waters to the sunlit surface, where photosynthesis can occur^{1–3}. How coastal upwelling regimes might change in a warming climate is therefore a question of vital importance^{4,5}. Although enhanced land–ocean differential heating due to greenhouse warming has been proposed to intensify coastal upwelling by strengthening alongshore winds⁶, analyses of observations and previous climate models have provided little consensus on historical and projected trends in coastal upwelling^{7–13}. Here we show that there are strong and consistent changes in the timing, intensity and spatial heterogeneity of coastal upwelling in response to future warming in most Eastern Boundary Upwelling Systems (EBUSs). An ensemble of climate models shows that by the end of the twenty-first century the upwelling season will start earlier, end later and become more intense at high but not low latitudes. This projected increase in upwelling intensity and duration at high latitudes will result in a substantial reduction of the existing latitudinal variation in coastal upwelling. These patterns are consistent across three of the four EBUSs (Canary, Benguela and Humboldt, but not California). The lack of upwelling intensification and greater uncertainty associated with the California EBUS may reflect regional controls associated with the atmospheric response to climate change. Given the strong linkages between upwelling and marine ecosystems^{14,15}, the projected changes in the intensity, timing and spatial structure of coastal upwelling may influence the geographical distribution of marine biodiversity.

Coastal upwelling is a major oceanographic current that is prominent near the eastern boundaries of both the Atlantic and Pacific basins. In these EBUSs, coastal upwelling arises when equatorward winds along the eastern flanks of the subtropical highs transport surface waters offshore, causing them to be replaced by cold and nutrient-rich waters from depth via Ekman dynamics (Fig. 1a). The enhanced nutrient supply to the euphotic zone generated by these coastal upwelling currents sustains several productive fisheries and marine ecosystems around the globe: the California Current System (CalCS), off western North America; the Canary Current System (CanCS), off northwestern Africa and the Iberian Peninsula; the Humboldt Current System (HCS), off western South America; and the Benguela Current System (BCS), off southwestern Africa (Fig. 1a and Extended Data Fig. 1). Taken together, these four EBUSs cover less than 2% of the ocean surface but contribute 7% to global marine primary production and more than 20% to global fish catches¹⁶. The EBUSs span a wide range of latitudes and are therefore spatially heterogeneous environments. At higher latitudes, coastal upwelling is characterized by a marked seasonal cycle with the upwelling season beginning in spring and extending through summer and early autumn, whereas the winter season is dominated by downwelling. The length of the upwelling season increases progressively as latitude decreases, with upwelling becoming mostly a year-round phenomenon at tropical–subtropical latitudes (Fig. 1b–e). The timing, duration and intensity of coastal upwelling are known to have a critical role in the phenology of key marine

ecosystem processes such as the recruitment of rocky intertidal organisms, and changes in these upwelling characteristics have been shown to cause substantial disturbances to ecosystems at multiple trophic levels^{2,3,17}.

Climate change is expected to affect coastal upwelling and, thus, marine ecosystems in the EBUSs^{4,5}. Bakun proposed a mechanism whereby greenhouse warming would intensify the summertime alongshore winds and coastal upwelling by strengthening the land–sea thermal difference and surface pressure gradient in upwelling regions⁶. Subsequent analyses based on historical observations and palaeoclimate reconstructions have found evidence for increased upwelling-favourable winds in some parts of the EBUSs^{8,18,19} but not in others^{10,20}, leading to disagreements about coastal wind trends across different data sources^{9,10}. Climate model studies on projected changes to coastal upwelling have also yielded inconsistent results^{11–13}. Thus, there seems to be considerable debate regarding the impact of climate change on coastal upwelling⁴. A recent retrospective meta-analysis partially addressed this controversy by showing that coastal upwelling has intensified over the past 60 years²¹. Here we present a complementary prospective analysis using state-of-the-art climate models to understand how coastal upwelling will change under future greenhouse warming over the course of the twenty-first century. We use offshore wind-driven Ekman transport as an index of coastal upwelling, and analyse historical and future simulations of 22 Earth system models developed for the Coupled Model Intercomparison Project phase 5²² (CMIP5) at multiple latitudes along the four EBUSs (Fig. 1a and Extended Data Fig. 1). These CMIP5 models reproduce the observed latitudinal variation in upwelling duration (Fig. 1b–e) and intensity (Fig. 1f–i) across all four EBUSs.

Considerable expansion of the upwelling season of several days per decade between 1950 and 2099 is evident at high latitudes in all four EBUSs (Fig. 2a, b). There are also noticeable differences between the Northern and Southern hemispheres and among the different EBUSs. The HCS and BCS in the Southern Hemisphere show larger and more consistent trends than do both the CalCS and the CanCS in the Northern Hemisphere. The trends in the Southern Hemisphere systems also increase with latitude and, in the case of the HCS, reach ~6 days per decade at the southernmost latitude, whereas the trends in the Northern Hemisphere systems vary non-monotonically with latitude by about 1 or 2 days per decade. Furthermore, the HCS and BCS exhibit trends of similar magnitude at common latitudes, whereas the CalCS and CanCS exhibit divergent trends. The positive trends are consistent and robust across models in the Southern Hemisphere systems, but inconsistent across models in the CalCS (Extended Data Fig. 3a–d). At lower latitudes, upwelling remains year-round between 1950 and 2099, and there is therefore no change in the duration of the upwelling season. Despite regional differences, the lengthening of the upwelling season at high latitudes in the EBUSs is a robust global response to greenhouse warming among the CMIP5 models. Both earlier onset and later termination of the upwelling season contribute comparably to the prolonged duration of seasonal upwelling in a warmer climate (Extended Data Fig. 2 and Extended Data Fig. 3e–l).

¹Sustainability and Data Sciences Laboratory, Department of Civil and Environmental Engineering, Northeastern University, Boston, Massachusetts 02115, USA. ²Department of Marine and Environmental Sciences, Marine Science Center, Northeastern University, Nahant, Massachusetts 01908, USA. ³Department of Integrative Biology, Oregon State University, 3029 Cordley Hall, Corvallis, Oregon 97331, USA.

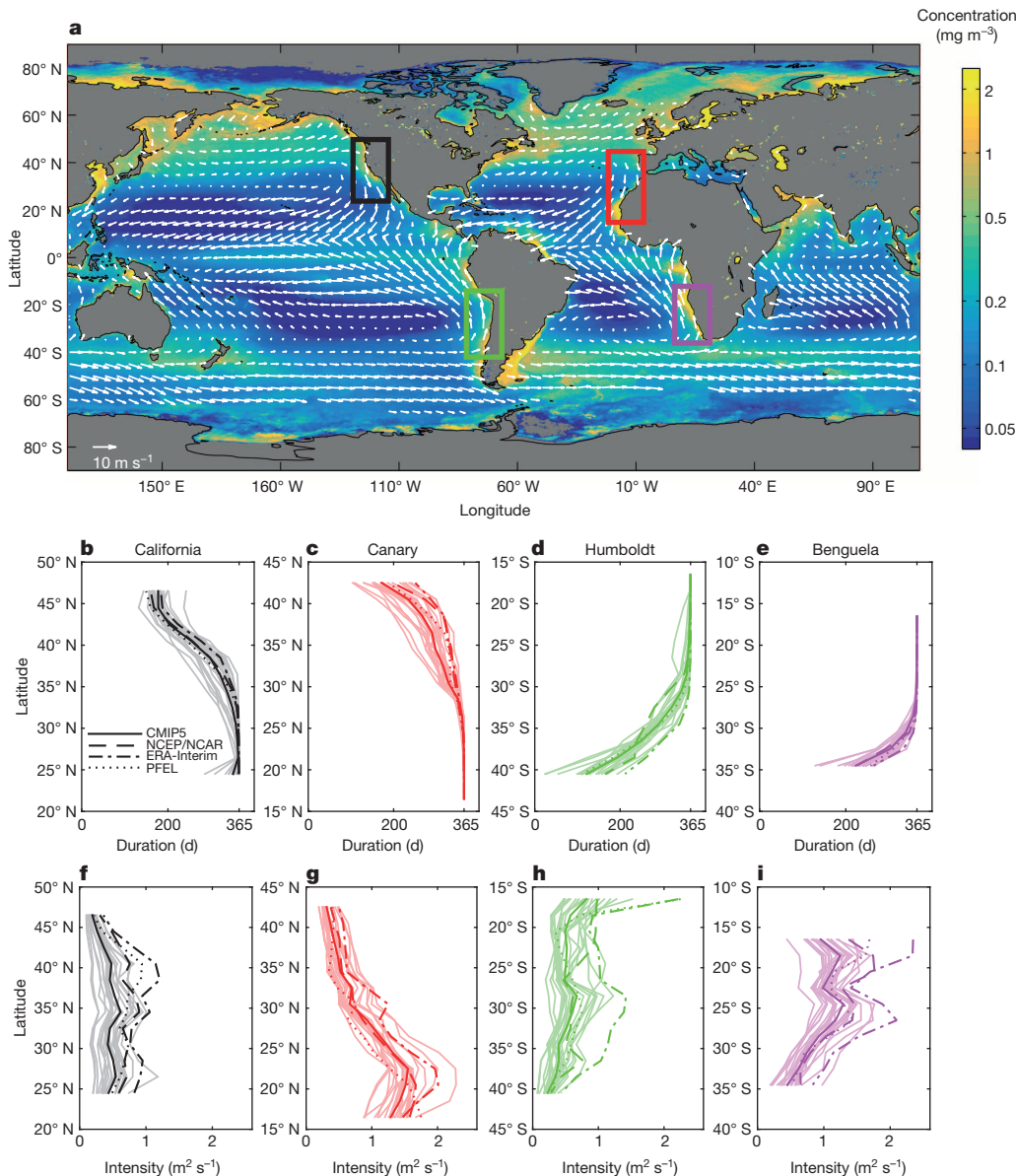


Figure 1 | Geographic locations of four EBUSs and latitudinal variations in coastal upwelling in each system. **a**, Aqua MODIS mean ocean chlorophyll *a* concentrations for 2002–2013 (colour scale; EBUS regions outlined with rectangular boxes) and mean QuikSCAT ocean surface vector winds for 1999–2009 (white arrows). **b–i**, Mean durations of the upwelling season (**b–e**) and

upwelling intensity (**f–i**) for individual CMIP5 models (thin lines). Also shown are the multimodel mean (thick solid lines), the NCEP/NCAR reanalysis (thick dashed lines), the ERA-Interim reanalysis (thick dash-dot lines) and the PFEL upwelling index analysis (thick dotted lines) for 1981–2005 in each EBUS.

Global warming also has a strong and consistent effect on upwelling intensity, which we define as the average offshore Ekman transport over the upwelling season. Between 1950 and 2009, the CMIP5 models show a strengthening of upwelling at higher latitudes in all EBUSs except the CalCS, and weakening upwelling at lower latitudes in the CanCS (Fig. 2c, d). In the CalCS, the upwelling intensity exhibits modest weakening trends that are robust at three latitudes. In the HCS, strengthening trends are present at all latitudes but robust only at the three southernmost latitudes. These greenhouse-warming-induced trends in upwelling intensity are consistent and statistically robust across the climate models in the CanCS and BCS and, to a lesser degree, in the CalCS and HCS also (Extended Data Fig. 3m–p).

The increased duration and intensity of upwelling at higher latitudes and the lack of such trends at lower latitudes will reduce the latitudinal gradient of upwelling in the EBUSs. To demonstrate this effect, we computed the spatial standard deviation of each upwelling metric to quantify changes in the spatial heterogeneity of upwelling between 1950 and

2009. Higher and lower spatial standard deviation values indicate greater and, respectively, lower spatial heterogeneity. The spatial standard deviation of the duration of the upwelling season exhibits decreasing trends in all four EBUSs (Fig. 3a). The trend is stronger and more consistent across the models in the Southern Hemisphere systems than in the Northern Hemisphere systems (Extended Data Fig. 5a–d), consistent with the larger magnitude of the latitudinal trends in upwelling duration in the HCS and BCS (Fig. 2a, b). Comparable decreasing trends are evident in the spatial standard deviation of the upwelling season onset and termination dates (Extended Data Fig. 4). A similar reduction in spatial heterogeneity is also predicted for the upwelling intensity in all four EBUSs (Fig. 3b). The decreasing trends in the spatial standard deviation of upwelling intensity are most pronounced and consistent among climate models in the CanCS, followed by those in the BCS (Extended Data Fig. 5m–p), in line with the strong magnitude of the latitudinal trends in upwelling intensity (Fig. 2c, d). The reduction in the spatial heterogeneity of these upwelling characteristics is less prominent

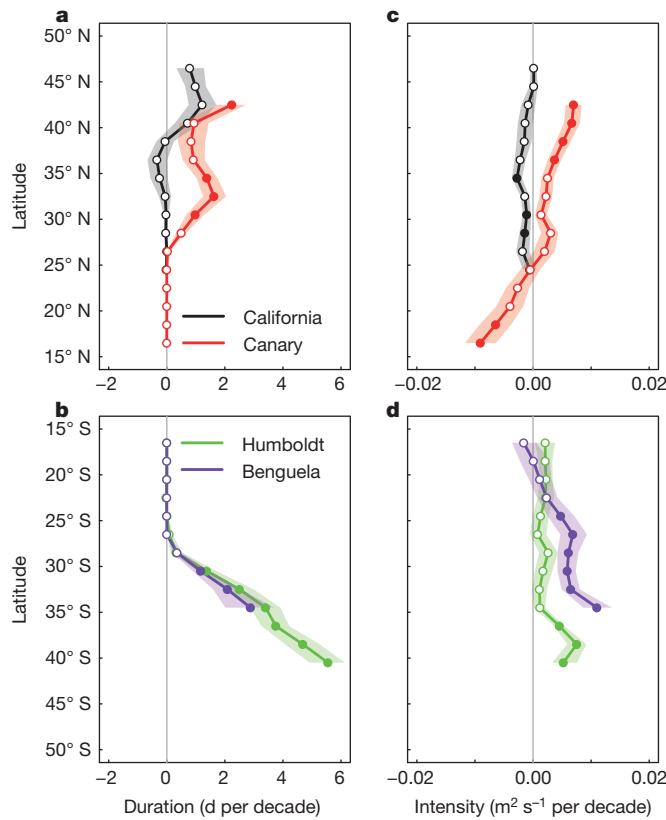


Figure 2 | Linear trends in upwelling duration and intensity. Multimodel means (solid lines) and 95% bootstrap confidence intervals (shading) of linear trends in upwelling duration (a, b) and intensity (c, d) for 1950–2099 for all four EBUSs. Filled circles represent trends that are robust across climate models (that is, at least 50% of the models show a statistically significant trend and at least 80% of those agree on the sign of the trend). The bootstrap confidence intervals are computed from 999 samples.

and robust in the CalCS and HCS. Nevertheless, the trend is statistically significant for half of the models and the multimodel mean (Extended Data Fig. 5).

The intensification of upwelling in both hemispheres over the course of the twenty-first century suggests that the underlying mechanism is related to global climate change. Bakun proposed that greenhouse warming would strengthen upwelling across the globe through differential land-sea surface heating because excessive summertime warming over land relative to the ocean intensifies the continental thermal lows adjacent to upwelling regions, thus increasing atmospheric pressure gradients and alongshore upwelling-favourable winds⁶. To test this hypothesis, we regressed the summertime upwelling intensity against the land-sea surface temperature difference at the high latitudes of the EBUSs between 1950 and 2099. Figure 4 shows that the increase in upwelling intensity is highly correlated with the increase in land-sea temperature difference in the CanCS, the HCS, the BCS and, to a lesser degree, the CalCS. This robust relationship between the land-sea temperature difference and upwelling intensity supports Bakun's hypothesis, and suggests a link between greenhouse warming and the intensification of upwelling. The increase in coastal upwelling under climate change is also linked to changes in upwelling phenology because the onset and termination of the upwelling season correspond to the times of the year when the wind-driven coastal current changes from downwelling to upwelling, and vice versa. Hence, the projected year-round increase in upwelling-favourable winds causes the upwelling season to start earlier, end later and last longer (Extended Data Fig. 7).

Although the latitudinal trends in upwelling intensification are generally consistent across regions, certain patterns are region-specific and

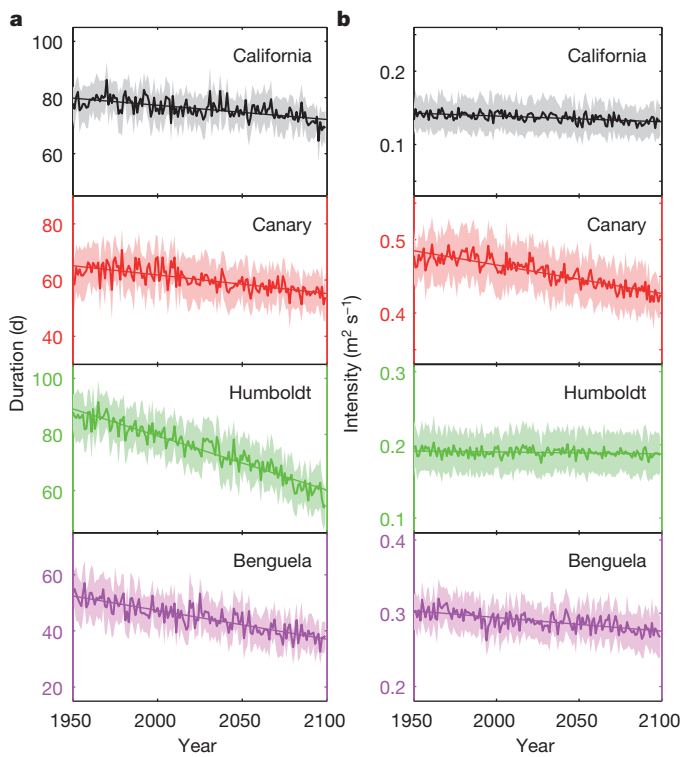


Figure 3 | Spatial standard deviations of upwelling duration and intensity. Multimodel means (thick lines) and 95% bootstrap confidence intervals (shading) of spatial standard deviation of upwelling duration (a) and intensity (b) for 1950–2099 for all four EBUSs. The thin straight lines indicate linear trends in the multimodel mean time series. The bootstrap confidence intervals are computed from 999 samples.

probably influenced by localized climate phenomena. For instance, the CalCS does not show intensification and the CanCS shows a robust weakening trend at the two lowest latitudes. Such differences among the EBUSs are probably the result of regional factors. Upwelling in the CalCS is strongly influenced by natural climate variability such as the El Niño/Southern Oscillation, Pacific Decadal Oscillation and North Pacific Gyre Oscillation^{23–26}, whose effects on upwelling may override those predicted by Bakun's hypothesis. In the CanCS, an increase in the land-sea thermal difference is expected to strengthen the southwesterly monsoon circulation that drives downwelling-favourable winds in the subtropics, a mechanism that may explain the reduction in upwelling intensity at low latitudes²⁷. Additionally, the poleward shift of subtropical anticyclones also tends to weaken upwelling-favourable winds at low latitudes²⁸. Describing how such regional processes interact with global greenhouse forcing will be critical to further resolve the dynamics of upwelling in a warming climate.

The lengthening and strengthening of upwelling at high latitudes and the resulting reduction in its latitudinal heterogeneity may have profound ecological impacts. On local scales, the climate-mediated intensification of upwelling could promote the productivity of fisheries and marine ecosystems by bringing more nutrient-rich waters to the surface, where they can subsidize the base of the food web⁴. Alternatively, the increased supply of such nutrient-rich and oxygen-poor waters from depth could have adverse effects on marine life by allowing hypoxic conditions to develop over large swaths of the coastal ocean and causing mass die-offs²⁹. These contrasting effects of upwelling intensification both depend on the continued delivery of nutrient-rich waters to the surface via upwelling. However, increased solar heating due to greenhouse warming could enhance stratification, deepen the thermocline and thus prevent cool and nutrient-rich waters from being upwelled^{4,30}. Such a decoupling of upwelling from the supply of nutrient-rich waters would jeopardize the persistence of fisheries and the functioning of marine ecosystems.

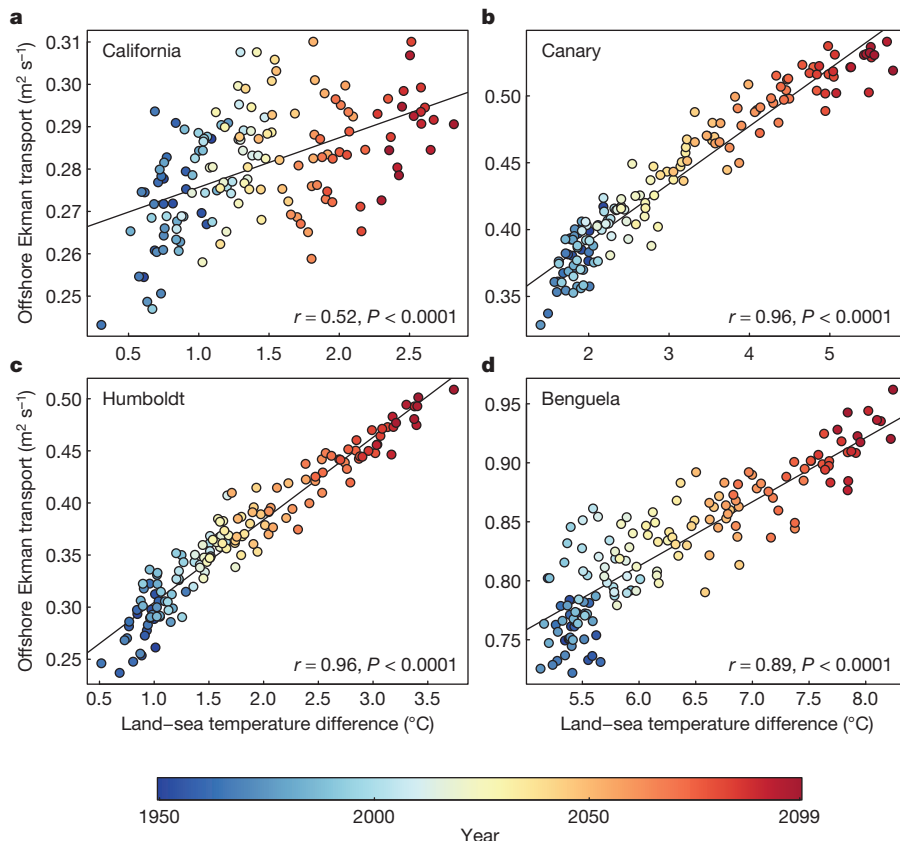


Figure 4 | Regression of summertime upwelling intensity against land-sea temperature difference. Scatterplots and generalized least-squares fits of multimodel mean summertime (May–September in the Northern Hemisphere and November–March in the Southern Hemisphere) offshore Ekman transport versus land-sea temperature difference for 1950–2099 at the three highest

latitudes in the CalCS (a), CanCS (b), HCS (c) and BCS (d). The correlations and corresponding *P* values between summertime upwelling intensity and land-sea temperature difference for individual models are tabulated in Extended Data Table 2.

On regional scales, the spatial structure of future upwelling trends is expected to alter the geographical distribution of species because both recruitment and biodiversity are strongly related to the existing latitudinal gradient in upwelling^{3,15}. Hence, by spatially homogenizing upwelling, climate change could remove an important environmental barrier associated with biodiversity, thereby increasing interspecific competition and species turnover in the coastal ocean. Overall, this suggests that the hotspots of climate-mediated change in upwelling identified here should be actively monitored to ensure the effective spatial management of productive fisheries and coastal ecosystems around the globe.

Online Content Methods, along with any additional Extended Data display items and Source Data, are available in the online version of the paper; references unique to these sections appear only in the online paper.

Received 30 July 2014; accepted 15 January 2015.

- Chavez, F. P. & Messié, M. A comparison of Eastern Boundary Upwelling Ecosystems. *Prog. Oceanogr.* **83**, 80–96 (2009).
- Barth, J. A. et al. Delayed upwelling alters nearshore coastal ocean ecosystems in the northern California current. *Proc. Natl. Acad. Sci. USA* **104**, 3719–3724 (2007).
- Menge, B. A. & Menge, D. N. L. Dynamics of coastal meta-ecosystems: the intermittent upwelling hypothesis and a test in rocky intertidal regions. *Ecol. Monogr.* **83**, 283–310 (2013).
- Harley, C. D. G. et al. The impacts of climate change in coastal marine systems. *Ecol. Lett.* **9**, 228–241 (2006).
- Doney, S. C. et al. Climate change impacts on marine ecosystems. *Annu. Rev. Mar. Sci.* **4**, 11–37 (2012).
- Bakun, A. Global climate change and intensification of coastal ocean upwelling. *Science* **247**, 198–201 (1990).
- McGregor, H. V., Dima, M., Fischer, H. W. & Mulitza, S. Rapid 20th-century increase in coastal upwelling off northwest Africa. *Science* **315**, 637–639 (2007).
- García-Reyes, M. & Largier, J. Observations of increased wind-driven coastal upwelling off central California. *J. Geophys. Res.* **115**, C04011 (2010).
- Narayan, N., Paul, A., Mulitza, S. & Schulz, M. Trends in coastal upwelling intensity during the late 20th century. *Ocean Sci.* **6**, 815–823 (2010).
- Barton, E. D. D., Field, D. B. B. & Roy, C. Canary current upwelling: more or less? *Prog. Oceanogr.* **116**, 167–178 (2013).
- Mote, P. W. & Mantua, N. J. Coastal upwelling in a warmer future. *Geophys. Res. Lett.* **29**, 2138 (2002).
- Snyder, M. A., Sloan, L. C., Diffenbaugh, N. S. & Bell, J. L. Future climate change and upwelling in the California Current. *Geophys. Res. Lett.* **30**, 1823 (2003).
- Wang, M., Overland, J. E. & Bond, N. A. Climate projections for selected large marine ecosystems. *J. Mar. Syst.* **79**, 258–266 (2010).
- Blanchette, C. A. et al. Biogeographical patterns of rocky intertidal communities along the Pacific coast of North America. *J. Biogeogr.* **35**, 1593–1607 (2008).
- Fenberg, P. B., Menge, B. A., Raimondi, P. T. & Rivadeneira, M. M. Biogeographic structure of the northeastern Pacific rocky intertidal: the role of upwelling and dispersal to drive patterns. *Ecography* **38**, 83–95 (2015).
- Pauly, D. & Christensen, V. Primary production required to sustain global fisheries. *Nature* **374**, 255–257 (1995).
- Iles, A. C. et al. Climate-driven trends and ecological implications of event-scale upwelling in the California Current System. *Glob. Change Biol.* **18**, 783–796 (2012).
- Gutiérrez, D. et al. Coastal cooling and increased productivity in the main upwelling zone off Peru since the mid-twentieth century. *Geophys. Res. Lett.* **38**, L07603 (2011).
- Santos, F., Gomez-Gesteira, M., DeCastro, M. & Alvarez, I. Differences in coastal and oceanic SST trends due to the strengthening of coastal upwelling along the Benguela current system. *Cont. Shelf Res.* **34**, 79–86 (2012).
- Lemos, R. T. & Pires, H. O. The upwelling regime off the West Portuguese Coast, 1941–2000. *Int. J. Clim.* **24**, 511–524 (2004).
- Synder, W. J. et al. Climate change and wind intensification in coastal upwelling ecosystems. *Science* **345**, 77–80 (2014).
- Taylor, K. E., Stouffer, R. J. & Meehl, G. A. An overview of CMIP5 and the experiment design. *Bull. Am. Meteorol. Soc.* **93**, 485–498 (2012).
- Schwing, F. B., Murphree, T., deWitt, L. & Green, P. M. The evolution of oceanic and atmospheric anomalies in the northeast Pacific during the El Niño and La Niña events of 1995–2001. *Prog. Oceanogr.* **54**, 459–491 (2002).
- Di Lorenzo, E. et al. North Pacific Gyre Oscillation links ocean climate and ecosystem change. *Geophys. Res. Lett.* **35**, L08607 (2008).

25. Chenillat, F., Rivière, P., Capet, X., Di Lorenzo, E. & Blanke, B. North Pacific Gyre Oscillation modulates seasonal timing and ecosystem functioning in the California Current upwelling system. *Geophys. Res. Lett.* **39**, L01606 (2012).
26. Jacox, M. G., Moore, A. M., Edwards, C. A. & Fiechter, J. Spatially resolved upwelling in the California Current System and its connections to climate variability. *Geophys. Res. Lett.* **41**, 3189–3196 (2014).
27. Cropper, T. E., Hanna, E. & Bigg, G. R. Spatial and temporal seasonal trends in coastal upwelling off Northwest Africa, 1981–2012. *Deep-Sea Res. I* **86**, 94–111 (2014).
28. Belmadani, A., Echevin, V., Codron, F., Takahashi, K. & Junquas, C. What dynamics drive future wind scenarios for coastal upwelling off Peru and Chile? *Clim. Dyn.* **43**, 1893–1914 (2014).
29. Grantham, B. A. et al. Upwelling-driven nearshore hypoxia signals ecosystem and oceanographic changes in the northeast Pacific. *Nature* **429**, 749–754 (2004).
30. Roemmich, D., & McGowan, J. Climatic warming and the decline of zooplankton in the California Current. *Science* **267**, 1324–1326 (1995).

Acknowledgements This work was funded by grants from Northeastern University's Interdisciplinary Research Program and the US National Science Foundation's Expeditions in Computing program (award no. 1029711). We acknowledge the World Climate Research Program's Working Group on Coupled Modeling, which is responsible for CMIP5, and we thank the climate modelling groups for producing and making available their model output. For CMIP5 the US Department of Energy's Program for Climate Model Diagnosis and Intercomparison provides coordinating support and led the development of software infrastructure in partnership with the Global Organization for Earth System Science Portals.

Author Contributions T.C.G., D.W. and A.R.G. designed the study. D.W. and T.C.G. analysed the data. D.W. wrote the initial draft of the manuscript with substantial contributions from T.C.G. All authors discussed and interpreted the results and edited the manuscript.

Author Information Reprints and permissions information is available at www.nature.com/reprints. The authors declare no competing financial interests. Readers are welcome to comment on the online version of the paper. Correspondence and requests for materials should be addressed to D.W. (dw2116@gmail.com).

METHODS

CMIP5 model simulations. We analysed the output of the historical simulations and RCP8.5 simulations from 22 CMIP5 models including (1) ACCESS1.0, (2) ACCESS1.3, (3) BNU-ESM, (4) CanESM2, (5) CMCC-CESM, (6) CMCC-CMS, (7) CNRM-CM5, (8) CSIRO-Mk3.6.0, (9) GFDL-CM3, (10) GFDL-ESM2G, (11) GFDL-ESM2M, (12) HadGEM2-AO, (13) HadGEM2-CC, (14) IPSL-CM5A-LR, (15) IPSL-CM5A-MR, (16) IPSL-CM5B-LR, (17) MIROC5, (18) MIROC-ESM, (19) MIROC-ESM-CHEM, (20) MPI-ESM-LR, (21) MPI-ESM-MR and (22) MRI-CGCM3, where the number in parentheses in front of each model name is the model index used in Extended Data Figs 3, 5 and 8. The model selection is based on the output availability of daily near-surface winds. From the official CMIP5 data portal (<http://pcmdi9.llnl.gov/esgf-web-fe/>), we retrieved daily near-surface (10 m) wind speed (*sfcWind*), zonal wind (*uas*), and meridional wind (*vas*) fields, as well as monthly surface temperature (*ts*) fields. The period analysed combines 1950–2005 from the historical simulations and 2006–2099 from the RCP8.5 simulations.

Offshore Ekman transport. We used daily offshore Ekman transport as an index of coastal upwelling, defined as the alongshore wind stress divided by the Coriolis parameter and seawater density. Because the CMIP5 multimodel ensemble does not provide output for daily or higher-frequency wind stress, we used the standard bulk aerodynamic formula to derive daily wind stress from CMIP5 daily near-surface wind speed, zonal wind and meridional wind with wind speed-dependent drag coefficient³¹. The near-surface winds were first projected onto the alongshore axis before being used to compute the alongshore wind stress via the bulk formula. In each EBUS, we compute daily offshore Ekman transport at an array of offshore locations evenly spaced by 2° in latitude and 1–2° (~100 km) from the coast (Extended Data Fig. 1 and Extended Data Table 1). Historical daily offshore Ekman transport values were also derived from the Pacific Fisheries Environmental Laboratory (PFEL) coastal upwelling index analysis³² and near-surface wind stresses from two atmospheric reanalysis products, namely the NCEP/NCAR reanalysis³³ and the ERA-Interim reanalysis³⁴. The PFEL coastal upwelling index has been extensively used to quantify coastal upwelling and its effects on fisheries and marine ecosystems at multiple trophic levels in the EBUSs^{3,15,17}.

Characterization of the phenology and strength of coastal upwelling. Following previous studies^{35,36}, we define the onset date, termination date, duration and intensity of the upwelling season as follows. We first computed the cumulative upwelling index (CUI) as the summation of daily offshore Ekman transport over a full year starting from boreal winter or austral winter, respectively 1 January and 1 July, at each latitude in the corresponding EBUSs. The onset of the upwelling season, also known as the spring transition, is the date on which the CUI reaches its annual minimum; likewise, the termination of the upwelling season, or the autumn transition, is the date on which the CUI reaches its annual maximum. The duration of the upwelling season is the total number of days between the onset date and termination date. The upwelling intensity is the average offshore Ekman transport over the upwelling season.

Relationship between the intensity and duration of coastal upwelling. Both upwelling intensity and duration are related to offshore Ekman transport, but in different ways. This is because upwelling intensity is defined as the ratio between cumulative Ekman transport during the upwelling season and the duration of the upwelling season, whereas upwelling duration is related to the time of the year when Ekman transport changes from being downwelling favourable to being upwelling favourable, or vice versa. Hence, for upwelling intensity to increase under climate change, the increase in cumulative Ekman transport over the upwelling season has to be greater than the increase in upwelling duration. If most of the increase in within-year Ekman transport occurs in the middle of the upwelling season, when Ekman transport is at its strongest, then there will be a tendency for upwelling intensity to increase but upwelling duration to remain the same. Conversely, if most of the increase in Ekman transport occurs at the onset or termination, when Ekman transport is at its weakest, then there will be a tendency for upwelling duration to increase but upwelling intensity to remain the same or even decrease.

Quantification of spatial heterogeneity of coastal upwelling. We quantified the spatial heterogeneity of the timing (onset and termination), duration and intensity of coastal upwelling in each EBUS and CMIP5 model using two different statistical measures. The first measure is the spatial standard deviation, which we defined for

each upwelling metric as $s = \sqrt{\sum_{i=1}^N (Y_i - \bar{Y})^2 / (N-1)}$, where Y_i is the value of the

upwelling metric at latitude i , \bar{Y} is the spatial mean of that metric averaged over all latitudes, and N is the number of latitudes in an EBUS. Large and small values of s are indicative of strong and, respectively, weak spatial heterogeneity, and an upward or downward trend in s represents increasing or, respectively, decreasing spatial heterogeneity. The second measure is the latitudinal slope coefficient, which we computed as the slope of a linear regression of each upwelling metric against the

absolute value of latitude in an EBUS: $\beta = \sum_{i=1}^N (X_i - \bar{X})(Y_i - \bar{Y}) / \sum_{i=1}^N (X_i - \bar{X})^2$. Here X_i is the absolute value of the i th latitude and \bar{X} is the absolute value of the average latitude in an EBUS. The values of β are typically negative for the duration and termination dates of the upwelling season and upwelling intensity because these metrics tend to decrease with latitude within an EBUS. Conversely, the onset date tends to increase with latitude, resulting in positive β values. For all the upwelling metrics, trends in β towards and away from zero are indicative of decreasing and, respectively, increasing spatial heterogeneity. Compared with the spatial standard deviation, changes in the latitudinal slope coefficient reflect variations in the large-scale gradient in coastal upwelling. Both approaches indicate that the intensity, duration, onset and termination of upwelling are all becoming less spatially heterogeneous over time within each EBUS (Fig. 3 and Extended Data Figs 4 and 6).

Trend analysis. We determined the 1950–2099 trends and their significance (P values) by regressing the time series of each upwelling metric and its spatial standard deviation against time by the generalized least-squares method. This method was used instead of the more traditional least-squares method to account for autocorrelation in the time series. A trend value is regarded as statistically significant if the associated P value is less than 0.05. To ensure that our results were not sensitive to the statistical approach used to estimate trends, we also used the Mann–Whitney U test to determine whether the 50-year median value obtained for each upwelling metric differs between 1950–1999 (historical) and 2050–2099 (RCP 8.5). We used the Mann–Whitney U test because the upwelling phenology data are generally not normally distributed. The generalized least-squares and Mann–Whitney U analyses yielded similar results, confirming the robustness of our conclusions (Extended Data Figs 3 and 8).

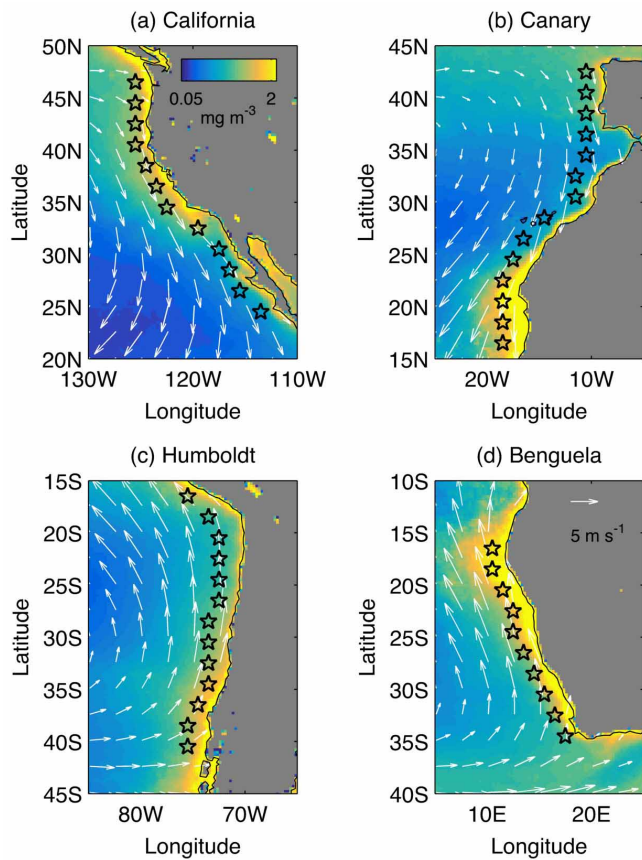
Robustness of upwelling trends across climate models. The projected changes in coastal upwelling reported in this study are based on an ensemble of 22 CMIP5 models. The robustness of these changes and our degree of confidence in them are commonly based on the level of model agreement³⁷. We quantified model agreement on upwelling trends using a method that assesses the degree of consensus based on both the statistical significance and the sign of the change³⁸. A change is interpreted as ‘robust’ when at least 50% of the models show a statistically significant trend and at least 80% of those agree on the sign of the trend. A trend is ‘not robust’ if (1) fewer than 50% of the models show statistically significant trend or (2) the majority of the models show a statistically significant trend but with low agreement on the sign of change. In this study, we chose to focus on the robust changes found in the majority of the EBUSs because they are most probably associated with global greenhouse warming.

Land–sea thermal difference and upwelling intensity. To determine the relationship between upwelling and land–sea thermal difference in the CMIP5 models, we computed the mean summertime (May–September in the Northern Hemisphere and November–March in the Southern Hemisphere) offshore Ekman transport over the three highest latitudes in each EBUS. We then determined the mean summertime land–sea surface temperature difference by computing the respective surface temperature differences between land and ocean averaged over a $10^\circ \times 5^\circ$ region centred on the coastline across the CalCS (119°W – 129°W , 42°N – 47°N), CanCS (4°W – 14°W , 38°N – 43°N), HCS (68°W – 78°W , 36°S – 41°S) and BCS (13°E – 23°E , 30°S – 35°S) for each year. Finally, we regressed summertime offshore Ekman transport against land–sea surface temperature difference using the generalized least-squares method. These analyses were conducted for both the multimodel mean and each individual CMIP5 model (Fig. 4 and Extended Data Table 2).

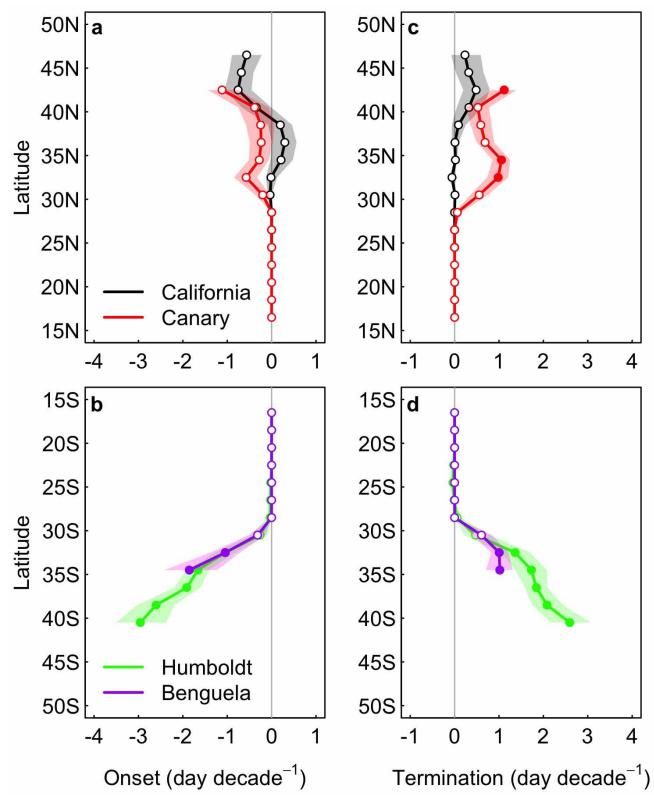
Coastal upwelling as a product of alongshore wind stress versus wind stress curl. Upwelling patterns in the EBUSs reflect both nearshore Ekman transport due to alongshore wind stress and offshore Ekman pumping due to wind stress curl^{39,40}. The typical spatial resolution of CMIP5 models is of the order of 100 km and is thus insufficient for resolving nearshore coastal upwelling patterns that occur within ~ 10 km of the coastline. Most existing studies, however, have used atmospheric observations or reanalysis products characterized by similar ~ 100 km resolutions to estimate coastal upwelling, and have successfully related these patterns to marine ecosystem functioning^{3,15,17}. The success of these low-resolution estimates of coastal upwelling may be attributable to their implicit integration of both nearshore Ekman transport and offshore Ekman pumping. Indeed, PFEL upwelling transport estimated from the 1° -resolution alongshore wind stress ~ 100 km offshore has a similar mean and variance to, and is highly correlated with, the total upwelling transport from a high-resolution (9 km) atmospheric model hindcast that comprises both nearshore Ekman transport due to alongshore wind stress and offshore curl-driven Ekman pumping⁴¹. This suggests that our CMIP5 upwelling estimates ~ 100 km offshore represent bulk upwelling transport that includes contributions from both nearshore Ekman transport and offshore Ekman pumping. Determining the relative contribution of these two processes to the overall patterns of upwelling will be an important next step for understanding how climate forcing influences both onshore and offshore oceanographic processes.

Data sources. Six-hourly US Navy Fleet Numerical Meteorology and Oceanography Center (FNMO) Ekman transport data at 1° spatial resolution used to compute the PFEL upwelling index were retrieved from <http://coastwatch.pfeg.noaa.gov/erddap/griddap/erdlasFnTran6.html> and averaged into daily means. Daily zonal and meridional wind stress data in the NCEP/NCAR reanalysis product at 2.5° spatial resolution were retrieved from <http://www.esrl.noaa.gov/psd/data/gridded/data.ncep.reanalysis.html>. Daily zonal and meridional wind stress data in the ERA-Interim reanalysis product at ~0.7° spatial resolution were retrieved from http://apps.ecmwf.int/datasets/data/interim_full_daily/. QuikSCAT climatological surface vector winds shown in Fig. 1 were retrieved from <http://cioss.coas.oregonstate.edu/scow/>. Aqua MODIS climatological chlorophyll *a* concentration data shown in Fig. 1 were retrieved from <http://oceanwatch.pifsc.noaa.gov/las/servlets/dataset?catitem=105>.

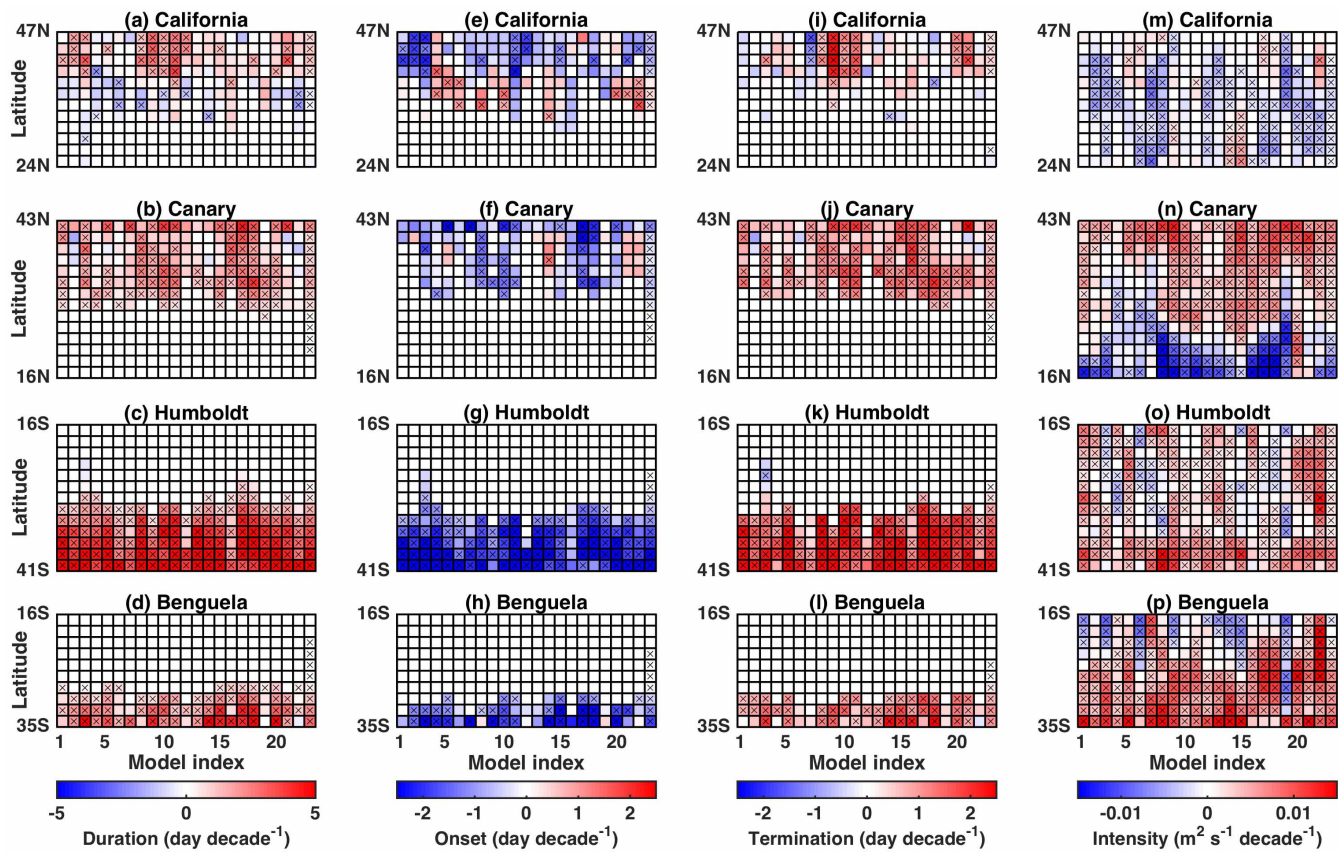
31. Trenberth, K. E., Large, W. G. & Olson, J. G. The mean annual cycle in global ocean wind stress. *J. Phys. Oceanogr.* **20**, 1742–1760 (1990).
32. Schwing, F. B., O'Farrell, M., Steger, J. M. & Baltz, K. *Coastal Upwelling Indices, West Coast of North America, 1946–1995*. NOAA Tech. Mem. NOAA-TM-NMFS-SWFSC-231 (US Dept of Commerce, 1996).
33. Kalnay, E. et al. The NCEP/NCAR 40-year reanalysis project. *Bull. Am. Meteorol. Soc.* **77**, 437–471 (1996).
34. Dee, D. P. et al. The ERA-Interim reanalysis: configuration and performance of the data assimilation system. *Q. J. R. Meteorol. Soc.* **137**, 553–597 (2011).
35. Schwing, F. B. et al. Delayed coastal upwelling along the U.S. West Coast in 2005: a historical perspective. *Geophys. Res. Lett.* **33**, L22S01 (2006).
36. Bograd, S. J. et al. Phenology of coastal upwelling in the California Current. *Geophys. Res. Lett.* **36**, L01602 (2009).
37. Collins, M. et al. in *Climate Change 2013: The Physical Science Basis* (eds Stocker, T. F. et al.) 1029–1136 (Cambridge University Press).
38. Tebaldi, C., Arblaster, J. M. & Knutti, R. Mapping model agreement on future climate projections. *Geophys. Res. Lett.* **38**, L23701 (2011).
39. Rykaczewski, R. R. & Checkley, D. M. Influence of ocean winds on the pelagic ecosystem in upwelling regions. *Proc. Natl. Acad. Sci. USA* **105**, 1965–1970 (2008).
40. Pickett, M. H. & Schwing, F. B. Evaluating upwelling estimates off the west coasts of North and South America. *Fish. Oceanogr.* **15**, 256–269 (2006).
41. Pickett, M. H. & Paduan, J. D. Ekman transport and pumping in the California Current based on the U.S. Navy's high-resolution atmospheric model (COAMPS). *J. Geophys. Res.* **108**, 3327 (2003).



Extended Data Figure 1 | Locations where daily offshore Ekman transport was computed along each EBUS. Also shown are Aqua MODIS mean ocean chlorophyll *a* concentrations for 2002–2013 (colour scale) and mean QuikSCAT ocean surface vector winds for 1999–2009 (white arrows) for the CalCS (a), CanCS (b), HCS (c) and BCS (d). The longitudes, latitudes and coast angles of all the locations (open stars) are given in Extended Data Table 1.

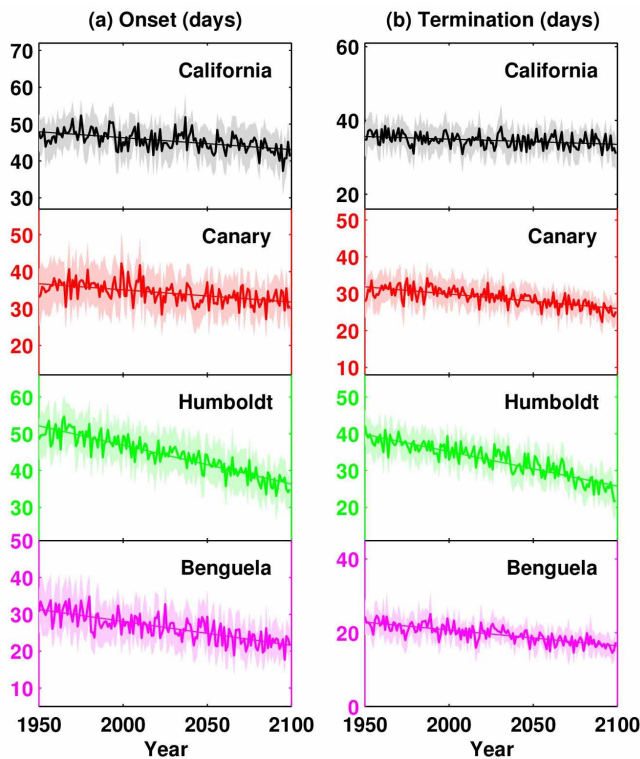


Extended Data Figure 2 | Linear trends in the timing of the upwelling season. Multimodel mean (solid lines) and 95% bootstrap confidence intervals (shading) of linear trends in the onset date (**a**, **b**) and termination date (**c**, **d**) of the upwelling season for 1950–2099 in all four EBUSs. Filled circles represent trends that are robust across climate models (that is, at least 50% of the models show a statistically significant trend and at least 80% of those agree on the sign of the trend). The bootstrap confidence intervals were computed from 999 samples.

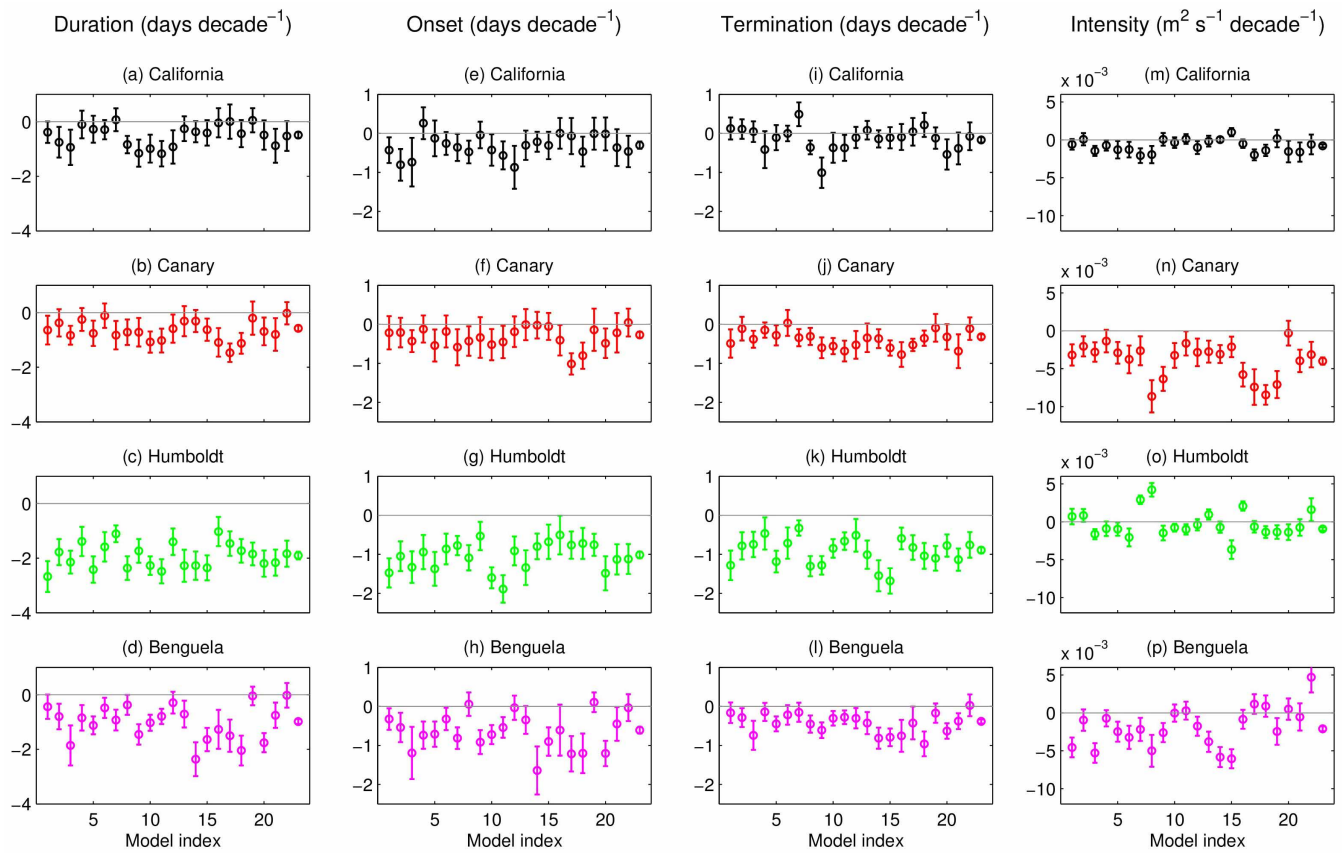


Extended Data Figure 3 | Linear trends in the upwelling metrics for the individual CMIP5 models. **a–d**, Generalized least-squares linear trends of upwelling duration for 1950–2099 in the CalCS (**a**), CanCS (**b**), HCS (**c**) and BCS (**d**). Red and blue respectively indicate positive and negative trend values. Crosses denote trend values that are statistically significant

(P value <0.05). The first 22 columns are 22 CMIP5 models; the last column is the multimodel mean. **e–h**, Same as **a–d** but for the onset date of the upwelling season. **i–l**, Same as **a–d** but for the termination date of the upwelling season. **m–p**, Same as **a–d** but for upwelling intensity.

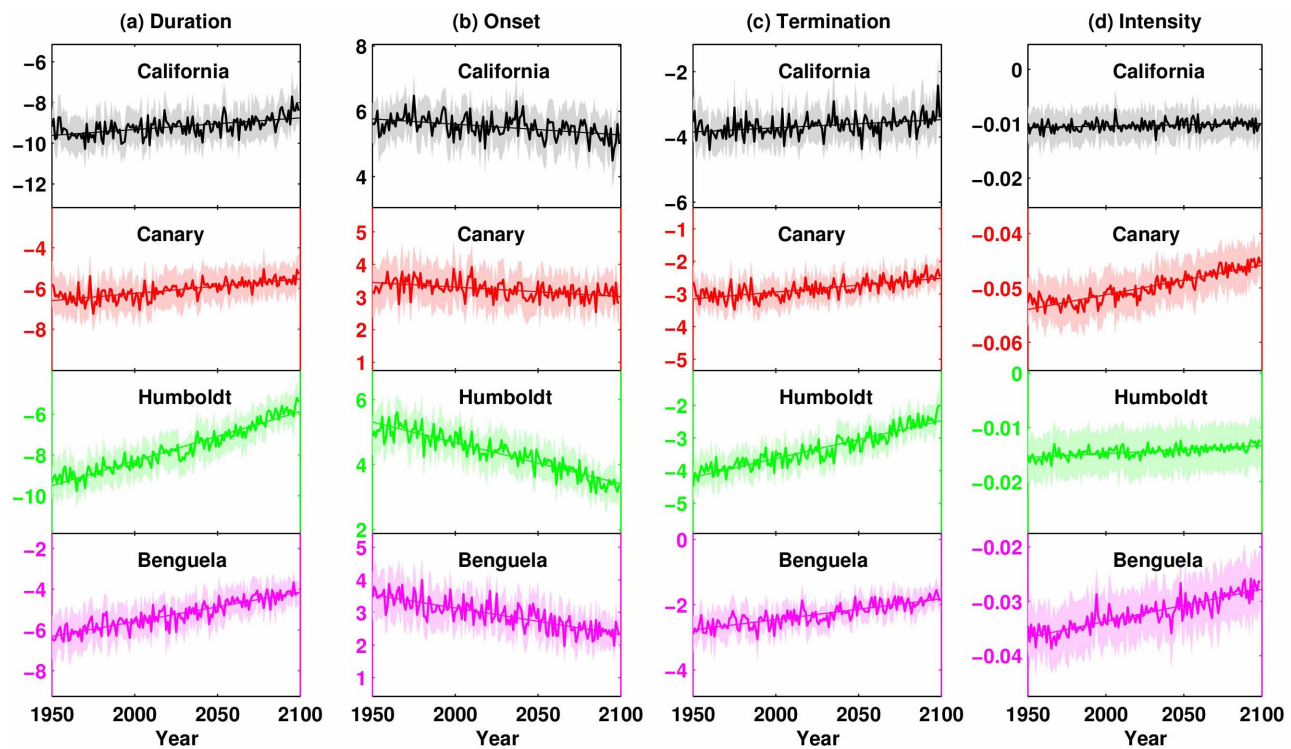


Extended Data Figure 4 | Spatial standard deviations of the timing of the upwelling season. Multimodel mean (thick lines) and 95% bootstrap confidence intervals (shading) of the spatial standard deviation of the onset date (a) and termination date (b) of the upwelling season for 1950–2099 in all four EBUSs. The thin straight lines indicate linear trends of the multimodel mean time series. The bootstrap confidence intervals are computed from 999 samples.



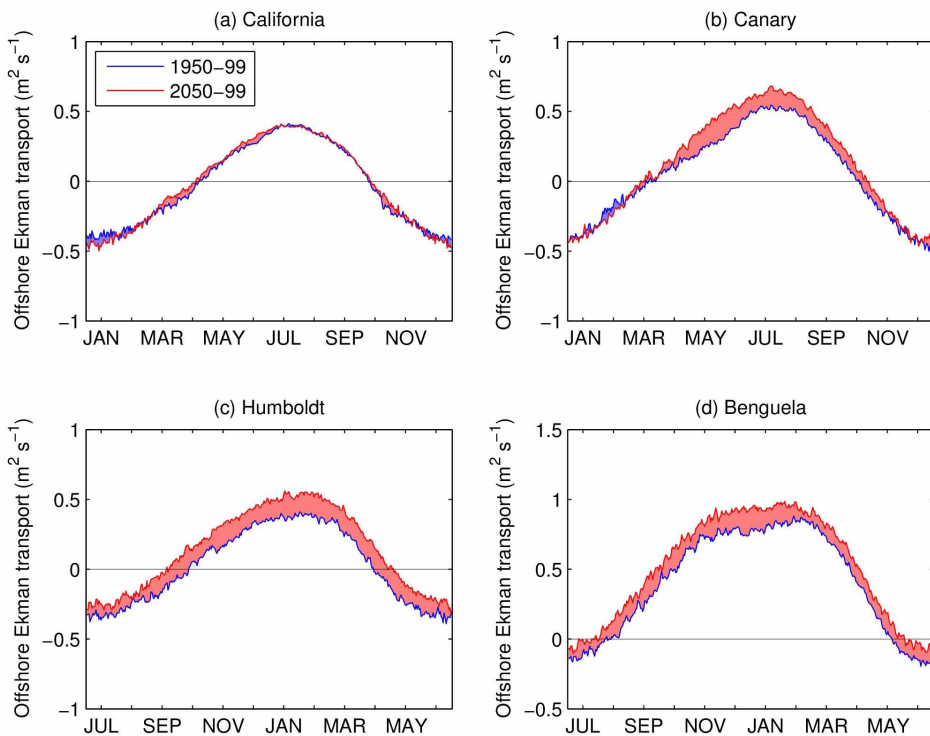
Extended Data Figure 5 | Trends in the spatial heterogeneity of coastal upwelling for individual CMIP5 models. **a–d**, Linear trends of the spatial standard deviation of the upwelling duration for 1950–2099 in the CalCS (**a**), CanCS (**b**), HCS (**c**) and BCS (**d**). Error bars indicate the 95% confidence

intervals. The first 22 bars are 22 CMIP5 models; the last bar is the multimodel mean. **e–h**, Same as **a–d** but for the onset date of the upwelling season. **i–l**, Same as **a–d** but for the termination date of the upwelling season. **m–p**, Same as **a–d** but for the upwelling intensity.



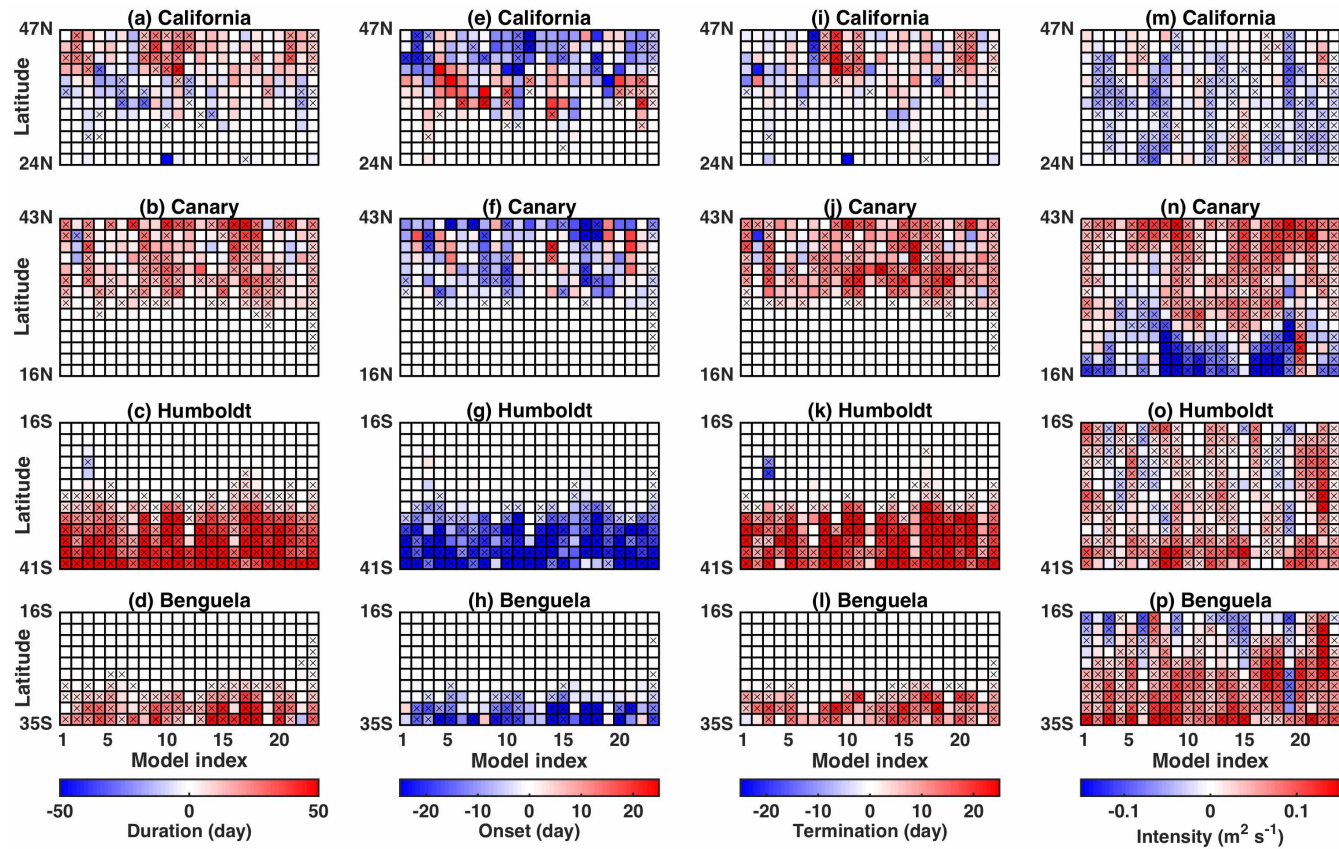
Extended Data Figure 6 | Latitudinal slope coefficients of upwelling metrics. Multimodel mean (thick lines) and 95% confidence intervals (shading) of the latitudinal slope coefficients of the duration (a; day per degree latitude), onset date (b; day per degree latitude) and termination date (c; day per

degree latitude) of the upwelling season, and of the upwelling intensity (d; $\text{m}^2 \text{s}^{-1}$ per degree latitude) for 1950–2099 in all four EBUSs. The thin straight lines indicate linear trends of the multimodel mean time series.


Extended Data Figure 7 | Intra-annual variation in upwelling trends.

Multimodel mean daily offshore Ekman transport for 1950–1999 (blue curve) and 2050–1099 (red curve) averaged over the three highest latitudes in the CalCS (a), CanCS (b), HCS (c) and BCS (d). Positive and negative temporal trends in the daily Ekman transport occur when the red curve is above and,

respectively, below the blue curve. These increases and decreases in upwelling transport are also highlighted by the red and, respectively, blue shading between the curves. The onset and termination of the upwelling season correspond to the times of the year when the daily Ekman transport first and, respectively, last reaches zero.



Extended Data Figure 8 | Median changes in upwelling metrics for the individual CMIP5 models. **a–d**, 50-year median change in the upwelling duration for 1950–1999 and 2050–2099 in the CalCS (**a**), CanCS (**b**), HCS (**c**) and BCS (**d**). Red and blue respectively indicate positive and negative trend values. Crosses denote changes that are statistically significant (P value <0.05)

according to the Mann–Whitney U test. The first 22 columns are 22 CMIP5 models; the last column is the multimodel mean. **e–h**, Same as **a–d** but for the onset date of the upwelling season. **i–l**, Same as **a–d** but for the termination date of the upwelling season. **m–p**, Same as **a–d** but for the upwelling intensity.

Extended Data Table 1 | Latitudes, longitudes and coast angles of the locations representative of the EBUSs

California			Canary			Humboldt			Benguela		
Latitude	Longitude	Angle	Latitude	Longitude	Angle	Latitude	Longitude	Angle	Latitude	Longitude	Angle
24.5°N	113.5°W	122.2	16.5°N	18.5°W	80.8	16.5°S	75.5°W	132.1	16.5°S	10.5°E	98.0
26.5°N	115.5°W	112.9	18.5°N	18.5°W	78.8	18.5°S	73.5°W	124.7	18.5°S	10.5°E	111.0
28.5°N	116.5°W	117.8	20.5°N	18.5°W	71.5	20.5°S	72.5°W	104.2	20.5°S	11.5°E	108.9
30.5°N	117.5°W	126.0	22.5°N	18.5°W	59.4	22.5°S	72.5°W	96.0	22.5°S	12.5°E	102.8
32.5°N	119.5°W	134.0	24.5°N	17.5°W	54.2	24.5°S	72.5°W	92.7	24.5°S	12.5°E	105.7
34.5°N	122.5°W	116.1	26.5°N	16.5°W	47.9	26.5°S	72.5°W	86.5	26.5°S	13.5°E	111.1
36.5°N	123.5°W	116.2	28.5°N	14.5°W	69.5	28.5°S	73.5°W	88.6	28.5°S	14.5°E	114.0
38.5°N	124.5°W	112.9	30.5°N	11.5°W	76.7	30.5°S	73.5°W	86.9	30.5°S	15.5°E	108.9
40.5°N	125.5°W	100.1	32.5°N	11.5°W	68.0	32.5°S	73.5°W	82.8	32.5°S	16.5°E	106.3
42.5°N	125.5°W	88.5	34.5°N	10.5°W	79.2	34.5°S	73.5°W	76.5	34.5°S	17.5°E	133.1
44.5°N	125.5°W	88.4	36.5°N	10.5°W	88.8	36.5°S	74.5°W	83.4			
46.5°N	125.5°W	109.9	38.5°N	10.5°W	88.3	38.5°S	75.5°W	92.7			
			40.5°N	10.5°W	85.2	40.5°S	75.5°W	97.4			
			42.5°N	10.5°W	61.4						

The coast angles are defined relative to the zonal axis pointing east and are used to compute the alongshore component of surface wind stress.

Extended Data Table 2 | Correlations between upwelling intensity and land–sea temperature difference for individual CMIP5 models in all four EBUSs

	California		Canary		Humboldt		Benguela	
	r	p-value	r	p-value	r	p-value	r	p-value
ACCESS1.0	0.17	4.2E-08	0.24	2.9E-10	0.65	7.1E-34	0.38	1.4E-15
ACCESS1.3	0.20	7.2E-24	0.29	8.1E-13	0.67	3.5E-37	0.14	3.9E-07
BNU-ESM	0.37	1.2E-16	0.19	4.9E-09	0.36	7.0E-15	0.32	1.1E-11
CanESM2	0.09	7.9E-06	0.32	8.4E-14	0.52	1.9E-25	0.27	2.4E-11
CMCC-CESM	0.29	8.4E-13	0.46	4.8E-22	0.52	2.5E-25	0.38	3.6E-16
CMCC-CMS	0.47	3.3E-22	0.27	6.1E-10	0.39	9.0E-17	0.02	9.7E-02
CNRM-CM5	0.16	2.2E-07	0.21	2.0E-09	0.67	1.7E-35	0.48	1.8E-20
CSIRO-Mk3.6.0	0.26	2.0E-11	0.16	3.0E-07	0.84	2.8E-59	0.43	2.3E-20
GFDL-CM3	0.39	7.5E-18	0.54	3.6E-26	0.73	2.8E-42	0.03	5.4E-02
GFDL-ESM2G	0.29	1.6E-12	0.36	6.3E-14	0.41	6.4E-18	0.04	3.4E-02
GFDL-ESM2M	0.41	2.2E-22	0.31	1.6E-12	0.47	2.2E-20	0.04	3.7E-02
HadGEM2-AO	0.02	1.0E-01	0.05	6.7E-03	0.40	5.2E-18	0.14	1.9E-05
HadGEM2-CC	0.11	2.3E-06	0.24	1.5E-09	0.59	1.8E-30	0.41	4.0E-17
IPSL-CM5A-LR	0.33	8.9E-16	0.60	2.6E-29	0.76	2.6E-45	0.69	3.9E-34
IPSL-CM5A-MR	0.22	9.9E-15	0.62	1.1E-34	0.73	2.5E-45	0.58	5.2E-31
IPSL-CM5B-LR	0.35	2.0E-15	0.41	2.7E-19	0.47	2.9E-22	0.30	3.5E-12
MIROC5	0.32	1.2E-13	0.54	8.9E-25	0.32	3.5E-13	0.14	7.0E-06
MIROC-ESM	0.33	2.2E-15	0.57	2.4E-26	0.46	5.2E-24	0.16	8.7E-07
MIROC-ESM-CHEM	0.07	8.0E-17	0.49	1.1E-22	0.56	2.6E-31	0.08	3.7E-04
MPI-ESM-LR	0.21	2.2E-09	0.45	2.9E-20	0.57	2.2E-28	0.25	2.2E-10
MPI-ESM-MR	0.23	6.9E-10	0.47	1.5E-22	0.60	1.5E-28	0.27	3.2E-11
MRI-CGCM3	0.36	1.4E-16	0.28	4.9E-13	0.47	1.4E-22	0.23	1.6E-10
CMIP5 MME	0.42	1.1E-07	0.94	9.1E-58	0.95	1.7E-70	0.90	7.4E-37

The correlation coefficients r and corresponding P values are estimated by the generalized least-squares method. The results for the multimodel mean are given in the last row.